*Revised Manuscript (Unmarked)
Click here to view linked References

Crossfibrillar mineral tessellation in normal and *Hyp* mouse bone as revealed by 3D FIB-SEM microscopy

Daniel J. Buss[a], Natalie Reznikov[b], Marc D. McKee[a,c*]

[a]Department of Anatomy and Cell Biology, McGill University, 3640 University Street, Montreal, Quebec, Canada H3A 0C7

[b]Object Research Systems Inc., Object Research Systems, 760 Saint Paul West, Montreal, Quebec, Canada H3C 1M4

[c]Faculty of Dentistry, McGill University, 3640 University Street, Montreal, Quebec, Canada H3A 0C7

***Corresponding author at:**

Marc D. McKee
McGill University
Strathcona Anatomy and Dentistry Building
3640 University Street
Montréal, Québec, Canada H3A 0C7

Email: marc.mckee@mcgill.ca

Running title: Mineral tessellation in bone

Keywords:

Bone, mineralization, X-linked hypophosphatemia (XLH), *Hyp* mice, osteocyte, mineral tessellation

This is the accepted manuscript of Buss DJ, Reznikov N, McKee MD. Crossfibrillar mineral tessellation in normal and Hyp mouse bone as revealed by 3D FIB-SEM microscopy. J Struct Biol. 2020 Nov 1;212(2):107603. doi: 10.1016/j.jsb.2020.107603

Highlights

- Mineral foci in bone grow as ellipsoids to produce crossfibrillar tessellation
- Mineral foci and ellipsoids in *Hyp* bone are stunted and show defective tessellation
- Defective tessellation patterns in *Hyp* bone likely compromise functional properties
- Osteocyte cell process morphology is altered in *Hyp* bone
- Deep-learning segmentation discriminates structural features in bone

Graphical Abstract

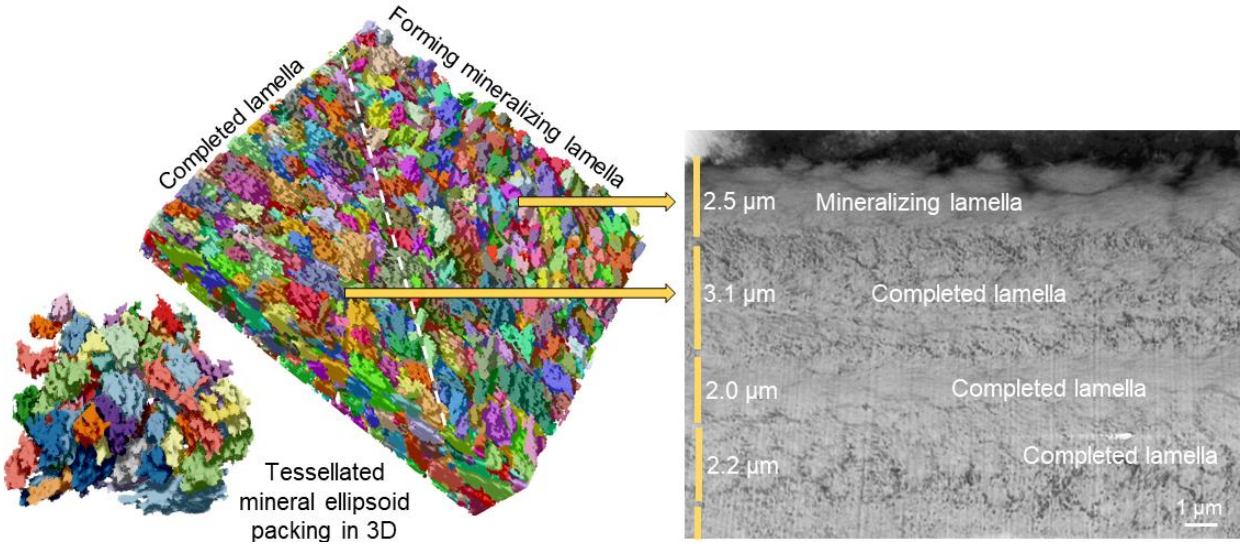

Abbreviations

ALPL:	Tissue-nonspecific alkaline phosphatase
ASARM:	Acidic serine and aspartate rich motif
CNN:	Convolutional neural network
FGF23:	Fibroblast growth factor 23
FIB-SEM	Focused-ion beam scanning electron microscopy
HAADF-STEM:	High-angle annular dark field scanning transmission electron microscopy
HPP:	Hypophosphatasia
Hyp:	Hypophosphatemic mouse model of X-linked hypophosphatemia
LCN:	Lacuno-canalicular network
OPN:	Osteopontin
PHEX:	Phosphate-regulating endopeptidase homolog X-linked
PP_i:	Pyrophosphate
ROI:	Region of interest
SIBLING:	Small integrin-binding ligand N-linked glycoprotein family
TEM:	Transmission electron microscopy
TNAP	Tissue-nonspecific alkaline phosphatase
TNSALP:	Tissue-nonspecific alkaline phosphatase
µCT:	Micro-computed tomography
WT:	Wildtype normal mouse
XLH:	X-linked hypophosphatemia

Abstract

In bone, structural components such as mineral extend across length scales to provide essential biomechanical functions. Using X-ray micro-computed tomography (µCT), and focused-ion beam scanning electron microscopy (FIB-SEM) in serial-surface-view mode, together with 3D reconstruction, entire mouse skeletons and small bone tissue volumes were examined in normal wildtype (WT) and mutant *Hyp* mice (an animal model for X-linked hypophosphatemia/XLH, a disease with severe hypomineralization of bone). 3D thickness maps of the skeletons showed pronounced irregular thickening and abnormalities of many skeletal elements in *Hyp* mice compared to WT mice. At the micro- and nanoscale, near the mineralization front in WT tibial bone volumes, mineralization foci grow as expanding prolate ellipsoids to abut and pack against one another to form a congruent and contiguous mineral tessellation pattern within collagen bundles that contributes to lamellar periodicity. In the osteomalacic *Hyp* mouse bone, mineralization foci form and begin initial ellipsoid growth within normally organized collagen assembly, but their growth trajectory aborts. Mineralization-inhibiting events in XLH/*Hyp* (low circulating serum phosphate, and increased matrix osteopontin) combine to result in decreased mineral ellipsoid tessellation – a defective mineral-packing organization that leaves discrete mineral volumes isolated in the extracellular matrix such that ellipsoid packing/tessellation is not achieved. Such a severely altered mineralization pattern invariably leads to abnormal compliance, other aberrant biomechanical properties, and altered remodeling of bone, all of which indubitably lead to macroscopic bone deformities and anomalous mechanical performance in XLH/*Hyp*. Also, we show the relationship of osteocytes and their cell processes to this mineralization pattern.

1. Introduction

Extracellular matrix mineralization is a fundamental process in Nature regulated by complex, and often redundant, mechanisms. These mechanisms have evolved over time, allowing for precise control of structure and form in the biominerals found within many organisms. In healthy bone, mineralization of the extracellular matrix confers stiffness and toughness when appropriately assembled and organized, and sufficiently mineralized. In disease, mineralization abnormalities can result in either hyper- or hypomineralized bones that are either brittle and easily fractured, or soft and deformed (with pseudofractures), respectively (1).

In bone mineralization, calcium and phosphate mineral ions combine through various precursor pathways to be deposited as crystallites of carbonate-substituted hydroxyapatite. Preventing (inhibiting) this mineralization pathway in soft tissues – where spontaneous pathologic crystal precipitation and growth would be debilitatingly destructive and often incompatible with life – are pyrophosphate molecules (PP_i) generated systemically from the hydrolysis of nucleotide triphosphates and other cellular metabolic processes (2-5). With most body tissues appropriately inundated by this ubiquitous and circulating inhibitory PP_i, mineralization is generally inhibited throughout the body, thus blocking a default pathway that otherwise would permit mineralization when appropriate levels of mineral ions are present, as they generally are. Other systemic inhibitors exist, such as the circulating protein fetuin-A made in the liver (6), and great strides have been made in understanding how these biomolecules work as systemic inhibitors of mineralization. In the context of PP_i activity, selective degradation of this inhibitory molecule in bones and teeth is required for mineralization to proceed (5), and is achieved through local expression of the ectoenzyme tissue-nonspecific alkaline phosphatase (TNAP, also known as TNSALP or ALPL) in the skeleton and dentition – this enzyme hydrolyzes PP_i, (3) – as the initial step in a process recently referred to conceptually as the *Stenciling Principle* of biomineralization (7), described in more detail below.

While type I collagen is the principal structural organic component of bone matrix, and by far the most abundant in terms of mass, noncollagenous proteins and small proteoglycans collectively are present at a similar molar ratio, and expectedly, appear to have key roles in biomineralization (8, 9). The SIBLING protein family (small integrin-binding ligand N-linked glycoproteins) of the bone noncollagenous proteins have a particular importance in the mineralization process of bones and teeth because of their high negative charge and intrinsic disorder, allowing for binding to free and complexed calcium (10). One SIBLING family member – the phosphoprotein osteopontin (OPN) – functions in part to inhibit mineralization locally within the extracellular matrix of bone (11-13). OPN and other SIBLING proteins have approximately one-quarter of their amino acids as calcium-binding, negatively charged (by

carboxylates) Asp and Glu, a protein net charge that can be further enhanced by post-translational phosphorylation of Ser residues (14). Dual inhibition of mineralization can be additionally achieved by the upregulation of OPN expression by PPi, contributing to overall inhibitory activity in the tissue, and as modulated by dephosphorylation of OPN via TNAP which reduces its inhibitory function (2, 11, 15). This seemingly counterintuitive role for OPN as an inhibitor within the normally mineralizing extracellular milieu of bone argues towards a more refined function for OPN relative to PP_i through gradual (*i.e.* the extended process of protein synthesis and secretion by exocytosis, coupled with progressive enzymatic degradation) and sustained restriction of the extent of mineralization – as might occur, for example, where mineralization gradually encroaches towards cell-matrix interfaces (7, 16). Such critical interfaces for the regulation of mineralization in bone would include that between the osteocyte and its myriad cell processes interfacing with the OPN-rich *lamina limitans* (17) delimiting the lacuno-canalicular network, and that between bone-lining cells and the OPN-rich *lamina limitans* at the very surface of bone where osteoid mineralization eventually terminates (9).

In bones and teeth, an additional level of regulation of the extracellular matrix mineralization process is achieved through expression of the enzyme phosphate-regulating endopeptidase homolog X-linked (PHEX). This transmembrane enzyme functions through inactivating cleavage of its substrate – osteopontin – into small noninhibitory fragments (18), thus providing even further fine tuning of mineralization locally in the bone extracellular matrix. Taken together, these aforementioned levels of local cancellation of a more general inhibitory effect can be described as the hierarchical Stenciling Principle of the control of mineralization (7). This principle describes that there is initially a systemic prevention of default-pathway mineralization, with further downstream regulation by enzymes permitting (stenciling) mineralization by tissue-specific (bones and teeth) enzyme expression, which is then followed by local refinement (fine tuning) for optimal mineralization into forms and locations that provide for best mechanical performance.

Bone's hierarchical structure enables the merger of stiffness (the ability to withstand loading without macroscopic deformation) and toughness (the ability to dissipate impact energy without catastrophic failure) (19). These extraordinary properties – which are often mutually exclusive – originate from the scale of tens-to-hundreds of nanometers as exemplified by the intimate relationship between type I collagen fibrils and noncollagenous proteins, and the mineral with which they share more-or-less the same locale. Importantly, all these relationships occur within a hydrated environment and are facilitated by bound water (20-22). TEM investigations by Nylen, Scott, and Mosley originally described the relationship between collagen and mineral crystals within fiber gap/hole regions in mineralizing

turkey tendon (23). Around the same time, Ascenzi *et al*. reported on this process as it appeared in osteons, describing small foci of crystal inception originating in broad bands of the major collagen periods, and eventually growing in a manner which completely obscures fiber structure (24). Following this, Landis, Weiner, and Traub identified the nature of mineral precipitation and growth on arrays of organized collagen molecules – being both within and outside fibril gap/hole regions (25, 26). The confined geometries found within such an organized collagen fibril template are in fact thought to contribute towards decreasing the energy barrier for these nucleation events to occur (27), with recruitment of mineral ions facilitated by highly negatively charged and flexible noncollagenous proteins (28). This process also occurs in an extrafibrillar manner where the apatitic crystallites are often larger and somewhat curved/bent (29, 30), and where matrix vesicles may be active carrying mineral ions and the enzymatic machinery for mineralization. Additionally, extrafibrillar mineral is stabilized by noncollagenous proteins, citrate and water, all in a local environment where amorphous precursor states appear to play a large role (31-37). Mineralization events therefore appear to occur quite heterogeneously, likely explaining the "built-in" redundancy afforded by Nature for something as vital as the vertebrate skeleton and dentition.

At the scale of microns, healthy mature lamellar bone is characterized by 3D assemblies of mineralized collagen fibrils grouped into bundles, found to be ordered into gently twisting and directional arrays with similarly aligned mineral (38). Between adjacent bundles, at the interfaces of parallel arrays of bundles (interlamellar boundaries), and near osteocytes, disordered collagen exists in a more chaotic state in which it is common to find osteocyte cell processes, and, significant amounts of proteoglycans and other noncollagenous proteins. At this micron scale, arrays of similarly ordered collagen bundles are observed as lamellae, and the osteocyte network within its vast lacuno-canalicular network is prominent. Cell bodies of osteocytes exist within the mineralized matrix in the fluid-filled lacunae in which they reside. These cells also have long processes that lie within channels called canaliculi. Within the lacuno-canalicular network, through these narrow interfacial regions around cells and processes of more compliant fluid-filled matrix, otherwise nominal strains experienced by the tissue as a whole can be amplified and sensed by the osteocyte through a variety of mechanisms (39, 40) that lead to critical signaling between bone cells (to regulate bone remodeling, for example). Development and maintenance of the nano- and microscale dimensions of the mineralized matrix is therefore of utmost importance in not only ensuring function at any given point in time, but also in preserving key cell signaling pathways that govern the overarching homeostasis of this tissue over months and years.

Mineralization diseases with osteomalacia result from insufficient/deficient mineralization (hypomineralization) of the organic extracellular matrix, and they can be particularly severe. For example, hypophosphatasia (HPP) is an inherited genetic disorder characterized by inactivating mutations in the *ALPL* gene coding for the enzyme TNAP. With bone unable to rid itself of excess inhibitory PP_i in the absence fully functional TNAP, mineralization of the skeleton is considerably reduced, and the disease is often fatal if not treated by enzyme replacement therapy (41). In a different disorder – X-linked hypophosphatemia (XLH) – widespread osteomalacia is accompanied by a loss of fine tuning of mineralization at bone cell-matrix interfaces fails (42, 43). In this disease, inherited inactivating mutations of the *PHEX* gene result in severely hypomineralized bones and teeth (osteomalacia/odontomalacia) attributable to renal phosphate wasting (44). XLH patients, as well as the *Hyp* mouse model of this disease, present with short stature and bone deformities, with bowed legs, knock knees and atraumatic pseudofractures being common in the patients. *PHEX* is normally highly expressed by osteocytes, as well as by osteoblasts and odontoblasts. This transmembrane zinc metallo-endopeptidase regulates levels of the principal phosphatonin FGF23 and its substrate OPN (45). When PHEX activity is lost or decreased, increased levels of FGF23 result in decreased expression of class NaPi-IIa and NaPi-IIc renal transporters leading to phosphate wasting. Additionally, locally at the extracellular matrix level, in this absence or loss of PHEX activity, OPN (substrate for PHEX) accumulates at aborted/stunted mineralization foci in the osteoid, at bone interfaces such as at the mineralization front, and surrounding osteocyte lacunae and canaliculi in the lacuno-canalicular network (42). Accumulation of OPN at sites within the bone matrix correlates with hypomineralized peri-osteocytic lesions (POLs, “halos”) of unmineralized bone around osteocytes (42), this likely altering the magnitude of matrix strains that these cells respond to, and perhaps causing changes in bone remodeling and even FGF23 production.

In trying to understand how mineral propagates throughout extracellular matrices of healthy mineralized tissues, and how this is dysregulated in osteomalacic diseases, here we used a combination of focused-ion beam scanning electron microscopy (FIB-SEM) operating in serial-surface-view mode and 3D reconstruction with deep learning (convolutional neural network)-based segmentation to investigate mineral and matrix structure and relationships. More specifically we examined in detail the relationship of mineral with collagen bundles near the mineralization front in circumferential lamellar bone from normal (WT) and mutant (*Hyp*) hypomineralized mouse bone as a model for the osteomalacic disease XLH. Submicron-scale 3D analyses were also performed on osteocytes and their cell processes near the mineralization front to observe their relationship with mineral. Extending to the macroscale, and underlying bone’s essential functions, we also used X-ray micro-computed tomography (μCT) to compare

the full skeletons of WT and *Hyp* mice in 3D, which allowed for additional interpretation of the mechanistic basis for bone mineral hierarchical organization in health and disease.

2. Methods

2.1 Animals and sample preparation

Tibiae of normal male C57BL/6 wildtype (WT) and mutant *Hyp* mice with truncation in the *Phex* gene (aged 3.5-5 months) were dissected and trimmed to isolate the diaphysis. Initial 24 h fixation with 2% paraformaldehyde in 0.1 M Na cacodylate buffer was completed for all samples, followed by decalcification in 8% EDTA and 1% paraformaldehyde solution for select samples. All samples were stained with alcian blue for 4 h (pH 5.8) before a secondary overnight fixation in 4% glutaraldehyde.

After washing in 0.1 M Na cacodylate buffer, conductive staining was performed on all samples using repetitive exposure to osmium and thiocarbohydrazide ligand (OTOTO method). This repetitive exposure method was first used to "minimize charging within highly variable surfaces in vertebrate tissues" (46), subsequently for the staining of pollen for SEM (47), and then for the first time in decalcified bone for focused-ion beam (FIB)-SEM operating in serial-surface-view mode (see below) (38). Undecalcified samples were gradually dehydrated at room temperature to 100% acetone followed by infiltration and embedding in Epon epoxy resin. Dehydration for decalcified samples was accomplished at cryo temperatures by high-pressure freezing (Leica EM PACT2) and freeze substitution (Leica EM AFS2) followed by standard infiltration and embedding in Epon resin.

2.2 Focused-ion beam scanning electron microscopy (FIB-SEM) in serial-surface-view mode

Bone samples were analyzed by FIB-SEM microscopy operating in the serial-surface-view mode (also known as slice-and-view mode) using an FEI Helios Nanolab 660 DualBeam (Thermo Fisher Scientific). Embedded samples were trimmed, and light microscopy sections were used to define regions of circumferential lamellar bone near the bone surfaces of the diaphysis. The blocks were placed on a 45-degree holder and silver conductive paint was used around all nonimaging surfaces. Samples were sputter coated using a Pt target (Leica Microsystems ACE 600) to a thickness of 5 nm. FIB sectioning of each final volume was performed at a final probe current of either 2.5 or 0.79 nA, thus serially ablating 16-nm layers off the block face with sequential, iterative imaging performed with an SEM backscattered electron detector at 2 kV. A voxel size of 16 nm was used for all samples, obtaining data over volumes of 6000-9000 um^3.

2.2.1 Osteocyte segmentation and 3D reconstruction

Dragonfly™ image analysis and deep-learning software (version 4.1, Objects Research Systems Inc., Montreal, QC, Canada) was used to analyze all image data. Each of the SEM image stacks was registered with respect to similar features in adjacent slices using the "mutual info" tool. For segmentation of cell features, initial grayscale segmentation using the "range" tool was used, however, this nondiscriminatory technique is much less reliable when segmenting organic regions of interest due to its lower contrast ratio when compared to inorganic mineral within the same dataset. Even in the decalcified samples, grayscale values in UBYTE are limited, and delicate features such as cell processes and the *lamina limitans* of lacuno-canalicular network appear as similar values attributable to noncollagenous protein staining within the extracellular matrix. To most effectively deal with this issue, signal from the *lamina limitans* (as well as from other noncellular features such as cement lines/planes) were manually erased using the region-of-interest "ROI painter" brush, "smart grid", and "snap" tools on 10 pre-selected slices in each stack. Similarly, these tools were also used to add any areas of the cell body and processes that may have been originally excluded in segmentation of grayscale values. The corrected slices were then provided as training input for a convolutional neural network (CNN) using a default CNN architecture: U-Net with a depth of 5 layers and 64 convolutional filters per layer. This method of deep learning for segmentation is demonstrated as case studies in a review within this same special issue on mineralized tissues (48). The training set was partitioned into learning and validation subsets (80% and 20%) with data augmentation (1 iteration vertical and horizontal flipping). The training parameters were the following: patch size was 32, stride-to-input ratio was 1.0, batch size was 64, and the number of epochs was 50. Following an initial segmentation using this trained deep-learning model, another 10 slices were manually corrected and used for further training of the same CNN for an additional 50 epochs with the same parameters. Small disconnected noise of less than 100 nm^3 was excluded from the final segmentation using the "multi ROI analysis" operation. Subsequently, the final ROI was converted into a "mesh" with one round of smoothing, with spherical kernel size 3.

2.2.2 Mineral segmentation and 3D reconstruction

Mineral segmentation in undecalcified (mineralized) bone stacks was accomplished through global grayscale thresholding. Using the Boolean operation of subtraction, any remaining cell features that were distinguished via deep learning above were removed. The resultant ROI included all mineral formations, either discrete or confluent, as one target class – this is known as semantic segmentation. Volume thickness heatmaps were then constructed using the "volume thickness map" operation. To

create these maps, each mineral segmentation was simplified using the "smooth" operation, using k=3 for 5 rounds. Slight smoothing was necessary because of the heavy computational nature of this method. Construction of the volume thickness heatmap involves inscribing spheres of maximal possible diameters within the 3D foreground features. The range of the spheres' diameters is then color-coded between blue (smallest) to red (largest) using the "jet" look-up table. For the analysis of full mice (see below), this look-up table was modified across all samples to ramp nonlinearly in order to highlight all skeletal features (both normal and pathologic).

For analysis of the mineral tessellation pattern seen throughout the stacks of undecalcified WT bone, a small subset of 3 out of 1272 slices was corrected from the mineral segmentations. Despite these tessellations being apparent upon visual inspection of the raw data, simple grayscale segmentation was not robust enough to distinguish the small variations in grayscale values where tessellations abut. To generate an ROI of the actual tessellations, a CNN with the same architecture described previously was trained using the corrected subset. The training set was partitioned into learning and validation subsets (80% and 20%) with data augmentation (2 iterations of vertical and horizontal flipping). The training parameters were the following: patch size was 64, stride to input ratio was 0.5 (50% overlap of adjacent patches), and the number of epochs was 100.

The next task was to label each prolate ellipsoid as a unique object (also known as instance segmentation, as opposed to semantic segmentation). Thus far an ROI was created from the prior deep-learning segmentation, however, many adjacent ellipsoids, although discrete, still made contact at several points. Keeping those volumes intact while labeling each tessellation as unique would allow the opportunity to quantify their individual size, orientation, and location with respect to each other, and to other features in the bone such as collagen bundles. To perform this task, a "watershed transform" operation was performed. The ROI was inverted and a "distance heatmap" was created. From this map, cores or origins of each ellipsoid were selected using local thresholding. In the "watershed transform" operation, both the original segmentation and selected origins/seeds are used as input. Each individual label was expanded in 3 dimensions from the defined origin until it reached the boundary with an adjoining tessellated ellipsoid. Shadowing effects were used to highlight the texture and orientation of these 3D tessellations in certain figures. The labeled "multi ROI" of mineral ellipsoids that was generated from the watershed transform segmentation of mineralized WT bone (undecalcified sample) was further analyzed and sorted by aspect ratio distribution in the uppermost forming lamella with its mineralization front, and from the immediately underlying, completely formed and mineralized lamellae.

2.2.3 Analysis of collagen organization

Analysis of the sublamellar organization of collagen through each stack was completed using the Image J (Fiji) directionality plugin. Reznikov *et al*. 2013 originally used this method to describe the appearance of repeating sublamellar collagen domains – ordered and disordered motifs (38). This automated directionality analysis was based on gradient change of recognizable elements of similar thicknesses – the collagen fibrils. Output from this analysis was the average angular directionality of the fibrils in each slice, and their dispersion. High-dispersion values indicate a lack of fibril organization within any one slice.

2.3 X-ray micro-computed tomography (µCT)

In addition to the bone sample analyses described above, 3 whole WT and 3 whole *Hyp* mice were euthanized and whole mice were placed in 50 mL conical tubes with pre-drilled holes to allow for penetration and exchange of a solution of 4% paraformaldehyde and 1% glutaraldehyde in 0.1 M Na cacodylate, within a 1 L beaker in which they were suspended under agitation for 14 days. Mice were transferred to new dry tubes after 14 days and imaged by X-ray micro-computed tomography using an Xradia Versa 520 (Carl Zeiss Gmbh, Oberkochen, Germany). Scanning was performed with a 0.4x objective lens, 40 kV source voltage, LE1 filter, and exposure of 1 seconds per projection. Detector and source distances were optimized to create a voxel side length of between 30 and 35 µm for each mouse, with no binning. This small difference in pixel size, along with automated vertical stitching, was necessary to fit the larger full WT mouse projections onto the detector. Segmentation of whole bone (mineralized and unmineralized) was completed using Dragonfly™ software and a combination of global grayscale thresholding, "range tool", elimination of background noise via "multi ROI analysis", and elimination of noise from the conical tube (manually using the "shape" tool and "remove from ROI" option). Five rounds of object smoothing were used across each segmentation, with spherical kernel size 3. This is the minimum smoothing option, lowering the computational expense of generating the aforementioned volume thickness heatmaps for each mouse.

3. Results

3.1 Characterization of the *Hyp* skeletal phenotype in 3D

Fig. 1A and Movies SM1A-WT and SM1A-*Hyp* (Supp. Material) shows WT and *Hyp* mouse whole skeletons at different ages as observed in 3D by µCT. Segmented skeletons obtained from the reconstructed X-ray tomograms image stack are portrayed using a color-coded heatmap for bone thickness. Prominent general features of the mutant *Hyp* mice include smaller overall stature and a substantial degree of thoracic kyphosis. More specific abnormalities readily observed from the thickness maps include lower limb deformities presenting as shorter and thicker limb bones. Enlarging the hindlimb (Fig. 1B upper panels, and Supp. Material Movies SM1B-LowerLimb-WT and SM1B-LowerLimb-*Hyp*) and thoracic/forelimb skeletal elements (Fig. 1B lower panels, and Supp. Material Movies SM1B-Thorax-WT and SM1B-Thorax-*Hyp*) revealed extensive flaring and thickening of the metaphyses in *Hyp* mice, as frequently found in severe cases of XLH and being most evident in the tibia. In the forelimb/thorax region, a similar thickening of both the proximal and distal ulna and radius was evident in *Hyp* mice as compared to WT mice. Another deformity frequently observed clinically in both hereditary and vitamin D-deficient forms of rickets – the so-called rachitic rosary of the rib (49) – has to date only been poorly documented in the *Hyp* mouse (50), but is clearly evident here when rendered in 3D, and it was observed in all three of the mice examined (Fig. 1A right panel).

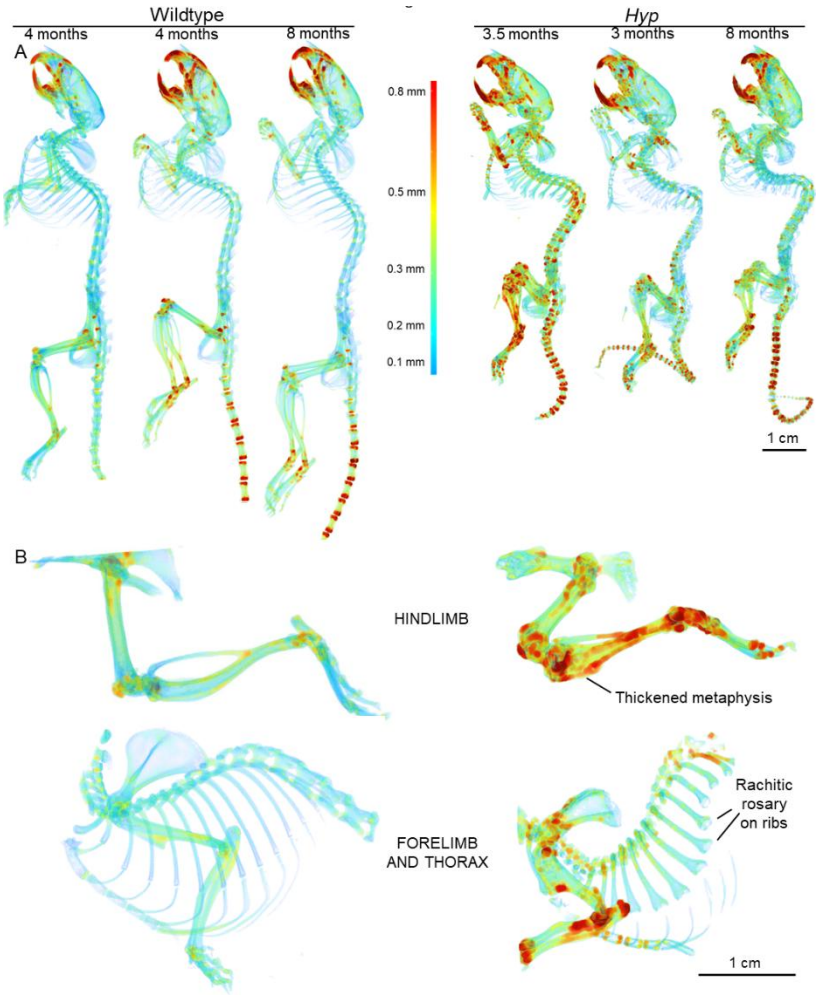

Fig. 1. **Volume thickness heatmaps of normal WT and mutant *Hyp* skeletons imaged by µCT**. Complete skeletons (A) and regional bones (B) of normal WT and mutant *Hyp* mice at different ages, as indicated, revealing the extent of the *Hyp* phenotype in terms of stature, deformities and thickness changes. Compared to WT mice, *Hyp* mouse skeletons are smaller, show prominent spinal kyphosis, have many long bones that are deformed and thickened with flaring metaphyses, including an obvious "rachitic rosary" of the ribs. See also Supp. Material Movies SM1A-WT, SM1A-*Hyp*, SM1B-HindLimb-WT, SM1B-HindLimb-*Hyp*, SM1B-Thorax-WT, and SM1B-Thorax-*Hyp*.

3.2 3D nanostructure of the mineralization front in the tibial diaphysis of normal WT and mutant *Hyp* bone

3.2.1 Mineral foci and mineral ellipsoids in WT and Hyp bone

As correlated with conventional light microscope histology of von Kossa (for mineral)- and toluidine blue (for counterstaining)-stained undecalcified tibial diaphysis (Fig. 2A and B), regions of WT and *Hyp* bone with a readily identifiable mineralization front (active bone formation site) were selected from these survey sections and were imaged in the FIB-SEM serial slice and view mode. After alignment

of SEM image slices, the morphological landscape near the mineralization front in the WT bone (Fig. 2C, E and G) appeared well organized and with a well-established osteoblast layer, osteoid, a few forming mineral foci, and a packed, irregular ellipsoidal-shaped pattern of contiguous but discrete elements emerging at the mineralization front. Movie SM2E (Supp. Material) shows in 3D – moving in an *en face* trajectory from the outermost osteoblast surface, through the osteoid and then mineralization front, and finally into the interior of fully mineralized bone. From this perspective, the mineralization pattern (bright areas) emerges gradually as small mineralization foci related to the organized collagen fibril bundles that then enlarge into ellipsoidal structures that coalesce at the mineralization front but retain their discrete boundaries deeper into the bone lamellae. This mineralization landscape is dramatically altered in *Hyp* mouse bone viewed the same way by examining the whole FIB-SEM stack (Fig. 2D, F and H, and Supp. Material Movie SM2F). In this state of hypomineralization in *Hyp* tibia where there is substantially more unmineralized matrix (osteoid), there was a striking large number of isolated mineral foci and mineral ellipsoids, that unlike in normal WT bone, showed a significant delay in coalescence and failed to form a distinct, coherent mineralization front. Eventually, deeper in the bone, substantial but irregular coalescence was achieved. Additionally, in Movie SM2F (Supp. Material), an osteocyte residing in its lacunae appeared near the end of the image stack. In both WT and *Hyp* bone, packed mineral ellipsoids (tesselles) retained discrete visible boundaries. Segmentation of mineral only (Fig. 2G and H) reveals the relative extent and depth of the aborted mineral ellipsoid landscape in the extracellular matrix in the mutant *Hyp* bone volume as compared to the normal WT bone volume (also see Supp. Material Movies SM2G and SM2H).

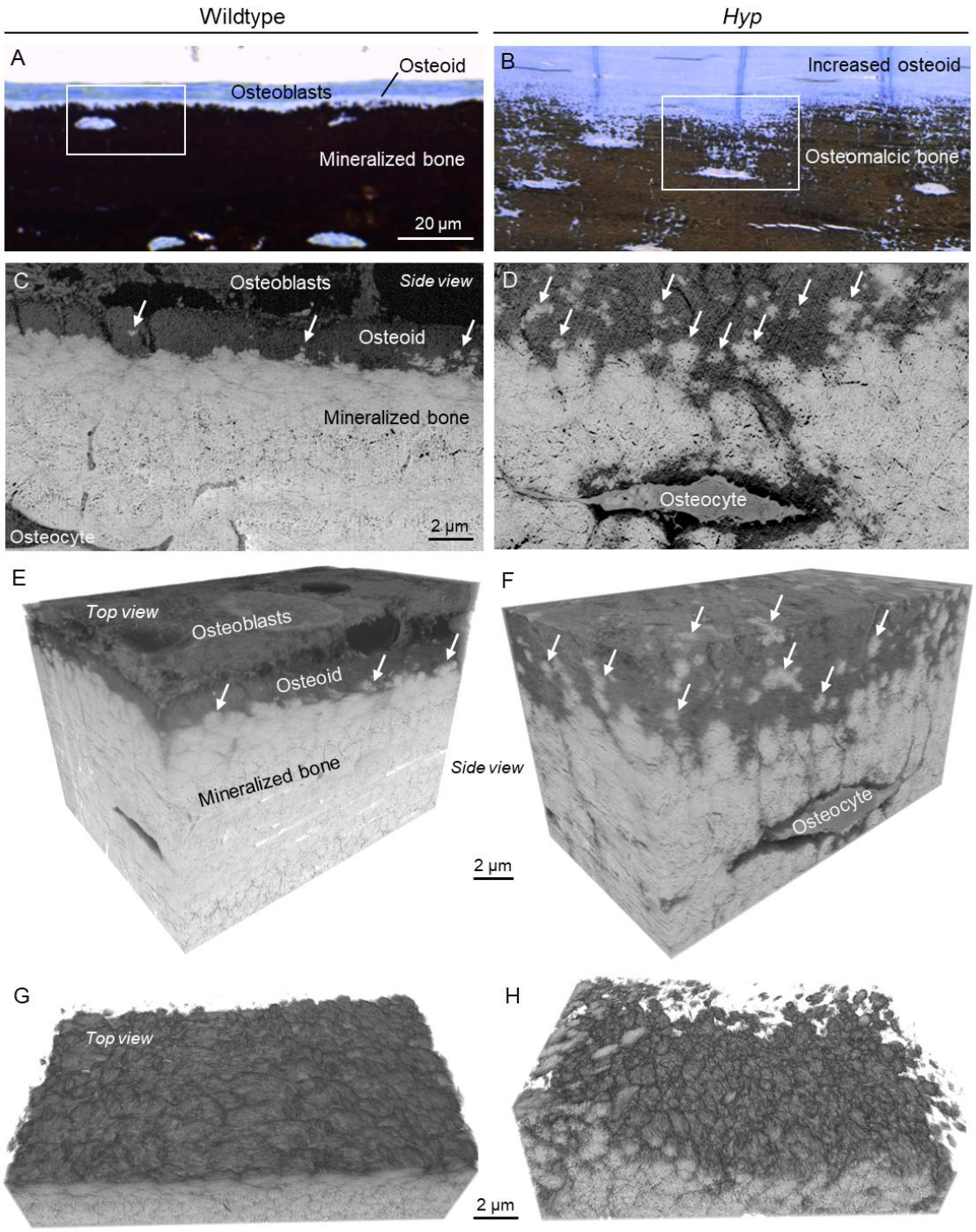

Fig. 2. **2D and 3D imaging of the mineralization landscape near the mineralization front at the tibial diaphysis in undecalcified normal WT and mutant *Hyp* adult mouse bone**. (A,B) Light microscopy of von Kossa- and toluidine blue-stained sections, and FIB-SEM (C,D) selected SEM images and (E-H) 3D reconstructions showing mineral ellipsoids (arrows) growing from mineral foci in the extracellular matrix near the mineralization front. Reconstructions G and H of mineral are after segmentation to exclude unmineralized matrix and cells from the dataset excluded (from the same datasets shown in C-F). Note the increased number of aborted and smaller mineral

foci/ellipsoids in the osteomalacic (hypomineralized) *Hyp* mouse bone. See also Supp. Material Movies SM2E, SM2F, SM2G and SM2H.

Using the thickness-mapping feature of the reconstruction software in which a progression of sphere-size fitting is used to establish relative thicknesses (here describing mineral volumes), mapped throughout the mineral segmentation, there was a median size of around 0.9 µm for the mineral ellipsoids in WT mouse bone (Fig. 3 left panel). In the *Hyp* bone sample, where progression (enlargement) of mineral volumes is impaired, the dispersion of the mineral component was again highly visible within the depth/thickness of the sample, and the median size of the spheres was approximately 0.4 µm, roughly half that of normal WT bone, and with few larger than 2 µm (Fig. 3 right panel). This *Hyp* sample thickness heatmap also reveals the presence of many aborted small mineral foci having measurements of only a few hundred nanometers (as also seen in Fig. 2D, F and H, and Supp. Material Movie SM2F).

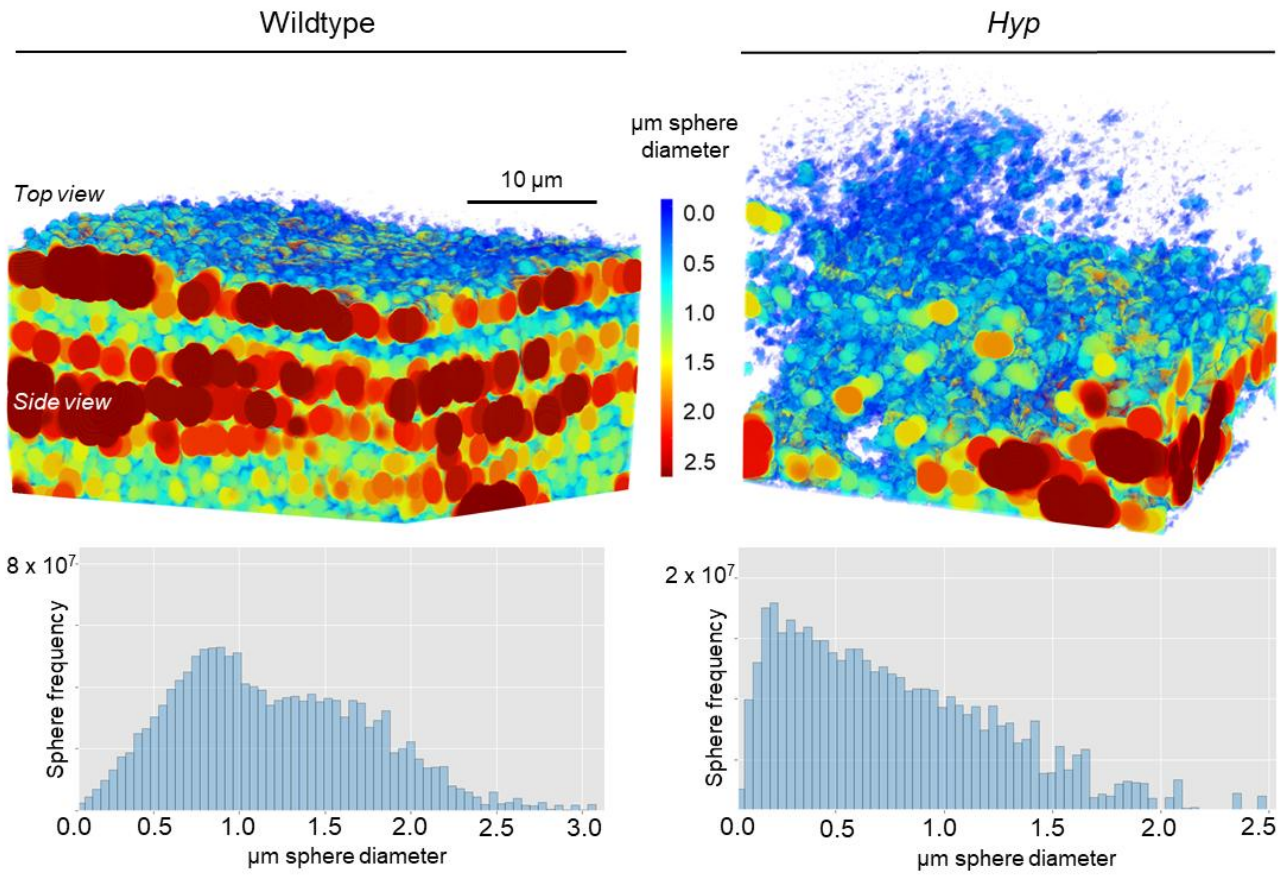

Fig. 3. **Volume thickness heatmaps and plots of mineral ellipsoids near the mineralization front of bone in the tibial diaphysis of normal WT and mutant *Hyp* mice**. Computational sphere fitting is applied by expanding spheres at random points in the dataset until a boundary is reached, at which time the sphere diameters are recorded and

color heatmapping is produced to describe the overall trajectory of mineral foci and mineral ellipsoid distribution and growth. Note the increased number of smaller ellipsoids in the *Hyp* mouse bone.

3.2.2 Mineral ellipsoids mature into crossfibrillar mineral tessellations

In normal WT tibia, mineral foci clearly show a progression into packed prolate ellipsoids (Fig. 2C, E and G, and Fig. 4A, C and E). Maturing ellipsoids in these images (white arrows) join a growing/coalescing mineralization front yet they remain slightly but distinctly discrete as abutting tessellation (ellipsoid packing) starts to occur. While many of these tessellations can readily be seen as distinct structures without any tagging/labeling or pseudocoloring, a CNN was trained to differentiate tessellations from the boundaries where lower grayscale values appeared. Following this, a watershed transform operation was applied to label each tessellation as a distinct region. The coloring scheme in Fig. 4 shows the results of this CNN segmentation, revealing distinct boundaries for all tessellations in normal WT bone (left panels), and the impairment that occurs in reaching a similar level of tessellation in the *Hyp* bone (right panels). The relation of mineral ellipsoids to collagen assembly can be seen in Fig. 5 and in Supplemental Material Fig. S1 for normal WT bone, and in Supplemental Material Fig. S1 for *Hyp* bone. There was no obvious difference in collagen bundle organization between WT and *Hyp* bone. For WT bone, bundles of around 1.5-2.5 µm at the mineralization front are described in Fig. 5A-D, with 5-10 mineral tessellations present in cross-section, or many tessellations along the length of a bundle. Tessellations and bundles having different orientation are shown through multiple lamellae in Fig. 5E and F. The lamellar period in which there is an observable change in this orientation appears as 2-3 µm (Fig. 5F).

Quantitative assessment of the aspect ratio of the mineral prolate ellipsoids after watershed segmentation as measured in normal mouse tibial cortical bone gave a mode aspect ratio of 2.05 (Supp. Material Fig. S2).

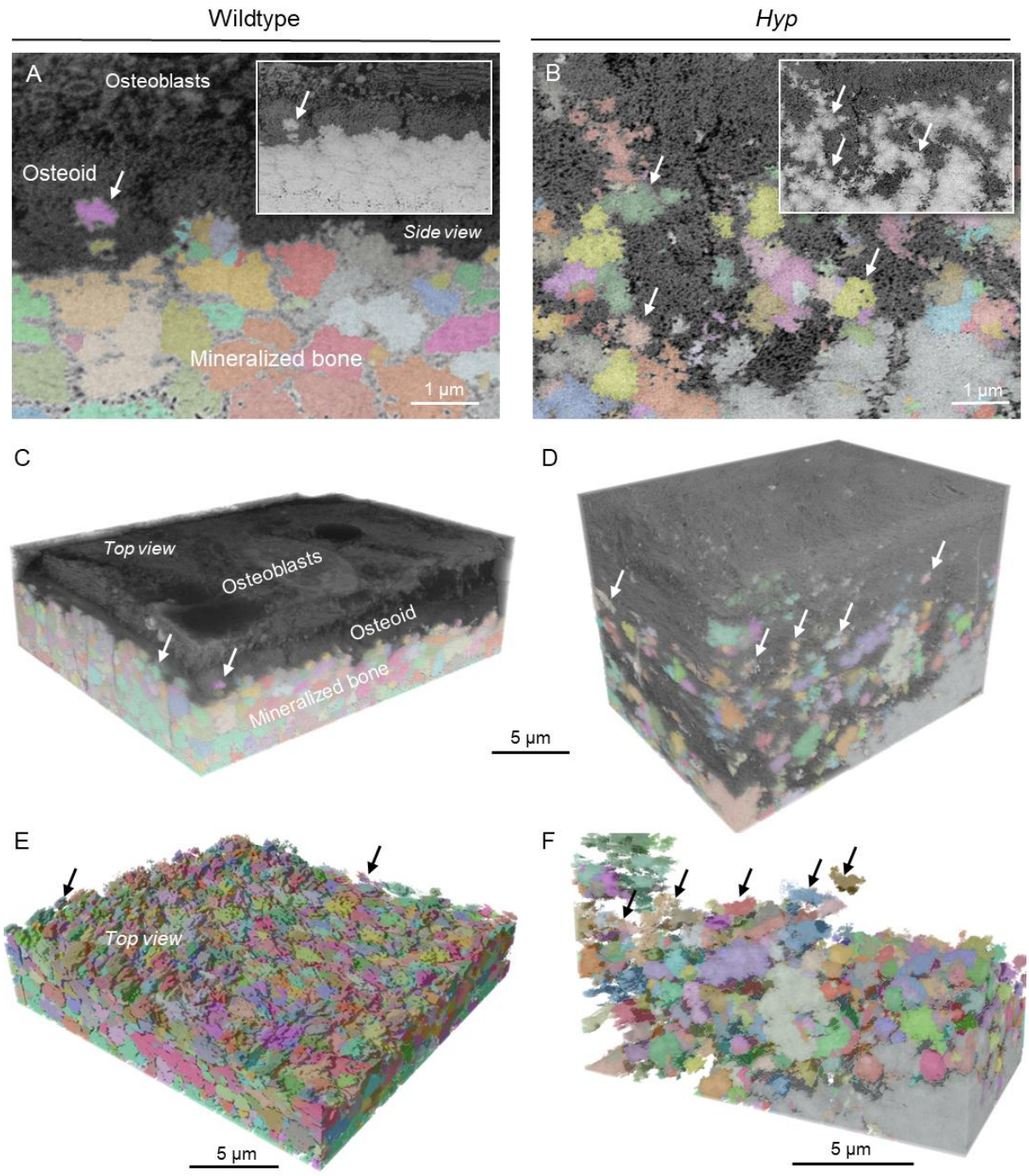

Fig. 4. **FIB-SEM reconstruction, segmentation, and labeling (coloring) of discrete and abutting mineral prolate ellipsoid volumes in undecalcified samples near and beyond the mineralization front in normal WT and mutant *Hyp* adult mice**. (A,C,E) In WT bone, mineral ellipsoids (arrows) deriving from mineral foci grow into irregular crossfibrillar tessellations (tesselles) whose packing can be observed across the entirety of the mineralization front volume. (B,D,F) In osteomalacic *Hyp* bone, there is defective growth, organization and packing of the mineral ellipsoids (arrows) with no contiguous mineral tessellation pattern occurring at this tissue depth within the tibia. Reconstructions E and F of mineral are after segmentation to exclude unmineralized matrix and cells from the dataset (from the same datasets shown in C and D).

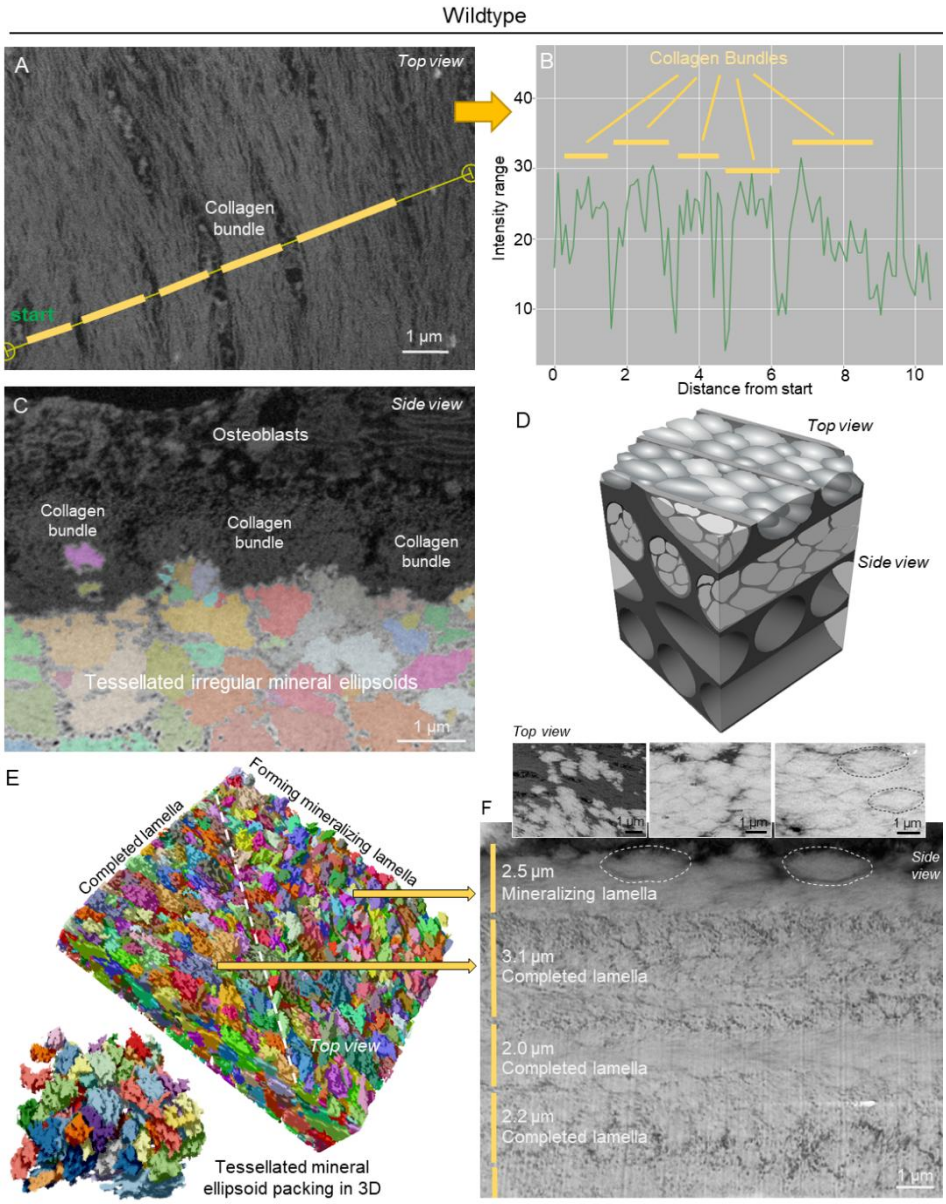

Fig. 5. Incorporation of crossfibrillar mineral tessellation within the lamellar structure of normal WT bone. (A,B) Assessment of collagen bundle thickness and spacing by intensity profiling after FIB-SEM. See also Supp. Material Movie SM5A. (C) Single FIB-SEM image showing the relationship between collagen bundles in cross-section and the pseudo-colored mineral tessellations that occupy their volume in mineralized bone. (D) Schematic diagram of the prolate mineral ellipsoid packing that provides crossfibrillar mineral tessellations occupying collagen bundles (here the collagen bundle volume dimensions are depicted as voids) that results in an adjacent lamellar offset by an indefinite angle. (E) Full segmentation and labeling/coloring of tessellations at the mineralization front within two lamellae, and a portion of this at higher magnification in the lower left corner. See also Supp. Material Movie SM5E. (F) Single SEM stack image of several bone lamellae from the side view near the mineralization front (osteoid towards top of the figure) where packed prolate ellipsoids/mineral tessellations can be readily seen either longitudinally or more-or-less in cross-section depending on the lamellar angle with respect to the imaging surface. Insets show top views likewise depicting prolate ellipsoids of mineral with their long axes aligned parallel to each other and to the long axis of the collagen fiber bundle within which they are situated; as mineralization proceeds, the ellipsoid growth trajectory packing progresses towards crossfibrillar tessellation. Dashed lines demarcate clearly

distinguishable, well-developed mineral ellipsoids. All samples are undecalcified to show both mineral and collagen relationships.

3.2.3 Observations on the osteocyte network

Additional tibial volumes slightly deeper (near or beyond the mineralization front) were obtained to study osteocytes in 3D in normal and osteomalacic *Hyp* bone. Since sample charging often occurs in the dual-beam microscope during FIB-SEM serial surface viewing, these samples were decalcified after conventional fixation to allow for better penetration of conductive osmium staining to reach osteocytes deeper in the bone. Fig. 6, along with Movies SM6A-WT and SM6A-*Hyp* (Supp. Material) shows the results from these analyses. Deep learning-based segmentation was used to discriminate osteocyte cell body and cell processes (labeled in blue); in the WT sample, cement lines/planes, and *lamina limitans* lining the lacuno-canalicular network, stained similarly and strongly with osmium (likely from the known accumulation of OPN at this site (9), and this imaging signal made segmentation difficult, so a deep-learning approach was applied (48). In both the WT and *Hyp* bone, cell processes radiated with an overall directionality towards bone surfaces. The WT osteocyte shown here (Fig. 6A-C left panels, and Supp. Material Movie SM6A-WT) had existed fully encased within mineralized matrix of its lacuno-canalicular location just beyond the mineralization front. For the *Hyp* osteocyte shown here (Fig. 6A-C right panels, and Supp. Material Movie SM6A-*Hyp*), although at approximately the same depth into the bone as its WT counterpart, the cell existed in the zone where only a diffuse mineralization front was present on account of the typical *Hyp* osteomalacia, and thus there is no well-defined outline of a lacuna and canaliculi. Remarkably visible in this EDTA-decalcified *Hyp* bone volume is the bright osmium staining dispersed throughout the matrix evidently arising from the original close association and co-localization of noncollagenous proteins with mineral and thus demarcating the mineral's previous locations (51) – this sometimes being referred to as a "crystal ghost" pattern (52). In Fig. 6B, the volume thickness heatmap operation (*i.e.* sphere fitting) of the software was applied as described previously to the cell processes (excluding the cell body) for each segmentation. From this analysis for these two cells – one each from normal WT and mutant *Hyp* bone – there was a clear difference in the size of the osteocyte processes, where the WT cell-process diameters were generally under 150 nm (except for a few converging nodal connections), whereas the *Hyp* cell-process diameters approached 400-500 nm in several cases, with most processes being over 200 nm. Selected images from the FIB-SEM stack are shown for both samples in Fig. 6C.

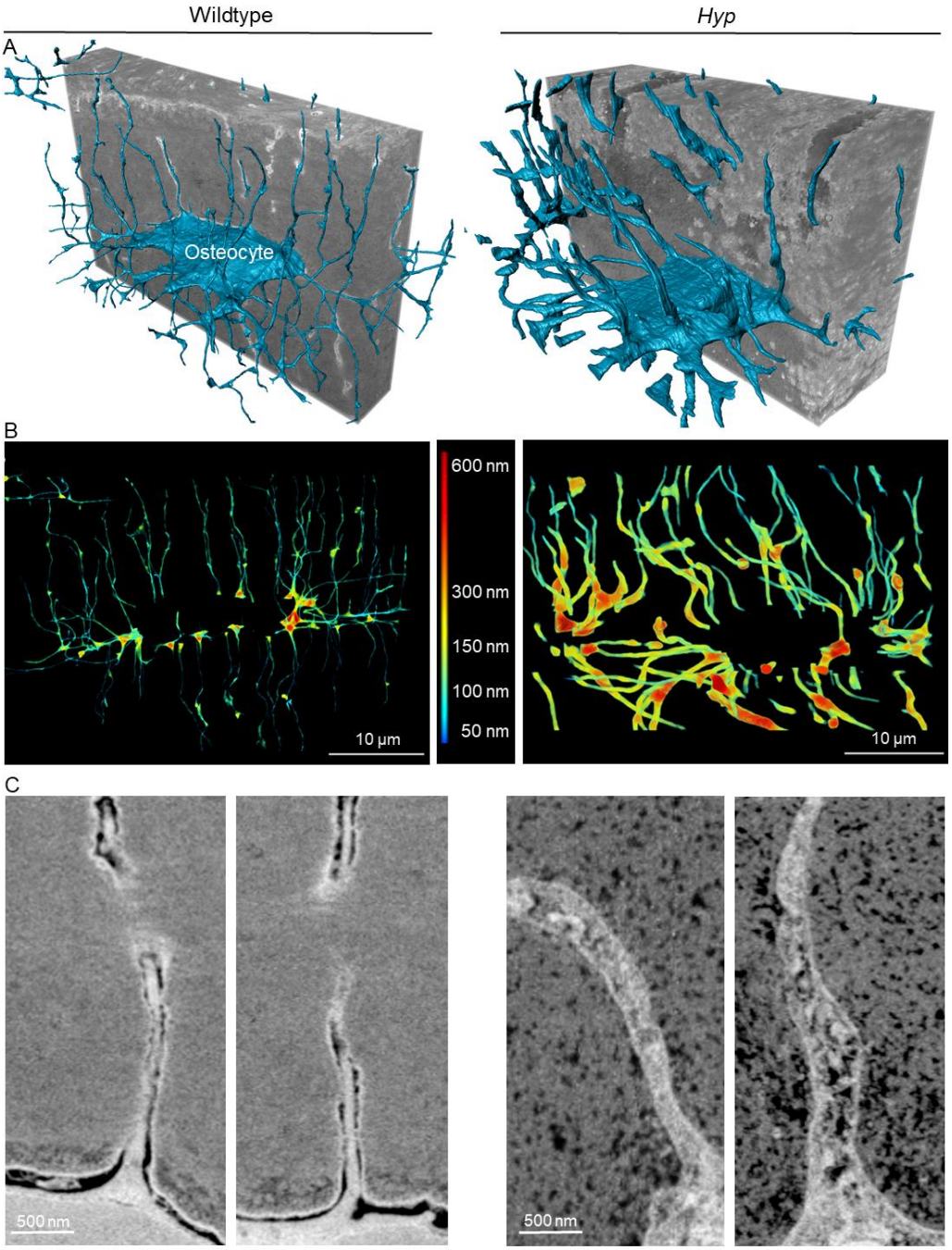

Fig. 6. **FIB-SEM reconstruction of the osteocyte network in the tibial diaphysis of normal WT and mutant *Hyp* adult mice**. (A,B) Deep learning-based segmentation of osteocytes and their cell processes (blue). Note the thickened cell processes in the *Hyp* osteocyte. Brighter regions are from osmium staining of noncollagenous protein accumulation in association with the defective mineralization landscape in these samples of decalcified *Hyp* bone, and the lacuno-canalicular system is not well-established in this region near the mineralization front, this differing significantly from the WT scenario. In WT decalcified bone, the brightest osmium-containing areas correspond to the *lamina limitans* layer delimiting the lacunar and canalicular walls, and a cement line/plane in the upper left corner. See also Supp. Material Movies SM6A-WT and SM6A-*Hyp*. (B) Volume thickness heatmaps of cell processes only after deep-learning segmentation showing thicker osteocyte cell processes in the *Hyp* bone sample. (C) Selected single SEM images of cell processes from normal WT and *Hyp* mice, again illustrating the increased thickness of the processes in the *Hyp* mice.

4. Discussion

Skeletal structure in vertebrates is a product of both inorganic and organic material constructed and shaped in response to biomechanical demands placed by evolutionary pressure. These demands have largely resulted in there being a balance between sufficient mechanical performance, with the energy cost of maintaining this biological infrastructure (19). Under normal physiological circumstances, precipitation, growth, and refinement of inorganic calcium phosphate as apatitic mineral deposited throughout bone's organic collagen matrix, together with considerable amounts of noncollagenous protein and water, allow for a stiff tissue that also displays considerable toughness. It is the arrangement and structure of these individual material components in the bone tissue that permit the diverse mechanical capabilities of the skeleton as a whole, and those of individual skeletal elements at different anatomical locations.

Diseases affecting bone in which there are alterations in the inorganic to organic material ratio, *i.e*. hyper- and hypomineralized bone, typically result in decreased mechanical performance. In osteogenesis imperfecta (so-called brittle bone disease) – a group of disorders characterized predominantly by collagen defects – there is impaired bone toughness and the brittle bone tissue frequently fractures under minimal mechanical loading (53). Hypermineralized bone has also been found in cases of osteoporosis, contributing to fracture risk in states of poor bone mass where toughness is already impaired (54). Conversely, hypomineralized osteomalacic bone fails because of excessive deformation and creep attributable to insufficient stiffness. In cases of rickets, abnormal levels of constituent mineral ions result in hypomineralization and growth plate abnormalities, with patients commonly having short stature and often bone deformities including *genu varum* (bowing of the legs) or *genu valgum* (knock knees) caused by plastic deformation of bones that are soft; other symptoms include, atraumatic pseudofractures, rachitic rosary of the ribs, and dental complications (55, 56).

With an inactivating truncation of the *Phex* gene (57), the skeletal phenotype of the *Hyp* mouse model phenocopies the osteomalacic inherited rickets disease X-linked hypophosphatemia (XLH). In examining the whole skeletons of these mutant mice by µCT and comparing them to normal WT mouse skeletons, and similar to what is seen in XLH patients, we show the expected smaller stature of these *Hyp* mice compared to their WT counterparts. Spinal abnormalities are a relatively common occurrence in XLH patients, and these likewise can be observed in *Hyp* mice (50). Here, in 3D from X-ray tomography, we corroborate the prominent kyphosis in these mice. Although this deformity appears to be poorly investigated in the context of rachitic disease, it may well occur from the thickening and/or fusion of vertebral bodies, as well as through enthesopathy at vertebral ligaments. Closer examination of individual bone anomalies in 3D, and using thickness maps for skeletal elements as generated by an application of

the software we used, we were able to observe the full extent of skeletal deformities across the whole *Hyp* skeleton. This included the prominent, XLH-characteristic "rachitic rosary" showing a flaring/thickening of the ribs at their costochondral joints. Increased and thickened bone was also seen at long bone metaphyses and joints, this generally being thought to be a compensatory feature that resists bending and torsional forces in a mineral-deficient state (58). In general, these various bone deformities in the *Hyp* mouse (and in XLH patients) may also be partly explained by disruptions in osteocyte-mediated mechanosensing arising from the well-documented peri-osteocytic lesions (POLs) where defective (hypo) mineralization increases matrix pliancy as sensed by osteocytes, and changes the degree to which strains are amplified into cues for bone remodeling (59).

This study was also undertaken to advance our understanding of the mechanistic basis by which mineral achieves its hierarchical organization in bone to provide it with its unique, resilient functional properties. Using the high-resolving power of FIB-SEM microscopy operating in serial-surface-view mode, we were able to reconstruct at the nano- and microscale mineral organization in 3D and in relation to collagen fibril bundles at the mineralization front in normal WT and mutant *Hyp* mouse bone. Physiologically, the initial growth of crystallites form small, generally spherulitic mineral foci ranging from tens-to-hundreds of nanometers in size both within fibrils and in the extrafibrillar space where specifically the negatively charged SIBLING family members (particularly OPN) have been precisely located (52, 60). Here, we build upon these 2D descriptions derived from conventional TEM micrographs to show in 3D how small nanoscale mineral foci enlarge to grow inside aligned collagen bundles forming bone lamellae, to transform into micrometer-sized, packed and tessellated prolate ellipsoids of mineral (tesselles). While early crystallite growth is known to exceed the confines of the gap zone/D-spacing and the lateral dimensions of typical collagen fibrils in bone (24, 61), much less is known about what happens thereafter in terms of foci growth. Here we describe how small, initially nano-sized mineral foci, being roughly spherulitic (at least in the interfibrillar compartment) transform to enlarge along one axis – in this case we observe elongation of the polar *c*-radius with respect to the equatorial *a*-radius – as prolate ellipsoids towards the mineralization front. Of note, the long axis of the parallel prolate mineral ellipsoids aligns with the long axis of the collagen fibril bundles – thus, like collagen, changing direction between adjacent bone lamellae. This aligned elongation axis of the mineral ellipsoids with collagen orientation likely arises from a lesser confinement effect along the long axis of the collagen fibrils and their bundles. The subsequent steps of this ellipsoid growth process are described as tessellation, and the details for this are given below in Section 4.1.

Mineralization foci growth is clearly regulated by OPN, where over many years we have used high-resolution colloidal-gold immunolabeling to document the intimate relationship of OPN to these foci (62). This early work has been supported by numerous *in vitro* and *in vivo* studies from our group and from others (notably from the Boskey, Hunter and Goldberg, Gower and Millan groups) showing the importance of OPN and its peptides in regulating the mineralization process, including work done in human patients (42). Of particular importance, OPN and its bioactive fragments have been shown to be physiologically relevant substrates for the PHEX enzyme produced by osteoblasts and osteocytes (18). PHEX enzyme essentially completely degrades OPN, gradually removing (inactivating) this mineralization inhibitor from the extracellular milieu allowing mineral growth to be carefully regulated, just as most intracellular pathways are carefully regulated. More specifically in this regard, where PHEX activity is absent or decreased (*Hyp*/XLH), OPN accumulates at aborted early mineralization foci, at the mineralization front, in the lacuno-canalicular network, and within peri-osteocytic lesions (18, 42). A similar pattern for OPN localization at the mineralization front is seen in osteomalacic FGF23-knockout mice having highly elevated OPN (13).

While osteomalacia in *Hyp* mice is widely known to result in part from poor systemic phosphate availability (and thus bone tissue phosphate availability) because of renal phosphate wasting caused by elevated circulating FGF23 produced by osteocytes, much less known is the role of OPN in inhibiting mineralization locally within the extracellular matrix (7). Here, it would be expected that such an accumulation of this inhibitory protein could affect mineral foci growth. In the present study we show in 3D the combined actions of low phosphate availability (low circulating serum phosphate) and inhibitory OPN accumulation on mineral foci that would otherwise (in normal bone) transform into packed irregular ellipsoids of mineral that ultimately tightly tessellate within the collagen bundles of lamellar bone. In *Hyp* bone, this tessellation transformation is apparently stunted by both the low serum phosphate and by the increased OPN, to the extent that incomplete tessellation takes place, and peri-osteocytic hypomineralized lesions occur. Indeed, in XLH patients given oral phosphate supplementation as a component of standard treatment, this combined effect might be enhanced by the known induction of OPN by phosphate (63, 64). Morphologically, related to altered mineral foci growth in hypophosphatemia, these findings advance earlier SEM work in which it was noted that “the mineralizing fronts of the bone from patients with hypophosphatemic rickets typically showed an unusually wide range of orientation of the unjoined mineral particle clusters” (43). In the present work we show, both quantitatively and visually in 3D, the extent of this impaired trajectory for mineral foci development in

Hyp bone that results in incomplete mineral ellipsoid tessellation at the altered mineralization front landscape characteristic of *Hyp*/XLH.

4.1 Crossfibrillar tessellation as a mineralization outcome of the packing of irregular mature prolate ellipsoids

As introduced above, the obvious disruption of mineral foci and ellipsoid growth and packing in *Hyp* mouse bone – attributable to low phosphate levels and increased inhibitory OPN – led us to further investigate this process of growth and fusion of mineral volumes under normal physiological circumstances. After looking at many samples of normal WT tibiae having smoothly milled (FIB) surfaces, a pattern was recognized near the mineralization front that extended into the bone across multiple lamellae. Mineral foci that had developed into mature ellipsoids and had joined the mineralization front appeared to remain slightly discrete with no complete fusion against adjacent abutting ellipsoids. This organization of abutting mineral volumes (irregular ellipsoids / tesselles) visible by eye in the microscope, formed the basis of what we now refer to as crossfibrillar tessellation. Using our 3D reconstruction deep-learning software, this pattern was recognized by a trained convolutional neural network (CNN) and was segmented over the full 3D analysis volume selected for the mineralization front. After applying watershed transformation for segmentation of these abutting tessellations, each were individually tagged (here shown with differing colors in our figures, but they can be readily seen even without coloring). Upon applying this same segmentation and labeling method to *Hyp* tibial bone, it was evident that there was much more spacing between the aborted mineral foci and the isolated mineral ellipsoids, as can even be observed by light microscopy. While some larger solid mineral volumes did appear, there was no *coherent* tessellation pattern visible within the analyzed volumes.

In surveying the literature, we were able to find some previously reported evidence (electron micrographs) of this crossfibrillar mineral tessellation. Using SEM, Bertazzo *et al*. noted similar "agglomerates of mineral plaques" in deproteinated rat femur and calvarial bone (65). Midura *et al*. likewise by SEM described "calcospherulites" in rat bone of similar appearance and size, being 0.5-1 µm in diameter (66, 67). More recently, Grandfield *et al*. reported on mineral "rosettes" in human femur where FIB sections viewed by HAADF-STEM seemed to match the appearance and size of the tessellations we describe when viewed perpendicular to the long bone axis (68). Finally, using SEM, Shah *et al*. reported on micrometer-sized, "marquise"-shaped motifs of bone apatite in rat calvaria (69). A similar pattern has also been noted previously for the distribution of organics (extracellular matrix) in decalcified bone that to

some degree reflects the mineral pattern that we describe as tessellations. Following from early reports of "mineral ghosts" (52) comprised of noncollagenous protein electron-dense staining in TEM corresponding to the general location, size and morphology of developing mineral foci, Reznikov *et al*. observed a differential intense staining "hour glass-like" pattern by FIB-SEM (70), again of similar dimensions to the crossfibrillar mineral tessellation pattern we report on here. Taken together, this evidence supports the notion that noncollagenous proteins (such as OPN enriched at these sites) regulate the formation of these µm-sized tesselles that have been reported by several groups in one way or another. Furthermore, dysregulation of this process in disease, for example by decreased phosphate availability and increased mineralization-inhibiting OPN (as in XLH/*Hyp*), would be expected to result in grossly inhibited mineral growth and organization (as we have documented here) leading to bone deformation and pseudofractures in osteomalacia. In Fig. 7, we summarize our understanding of the trajectory of mineralization events in WT and *Hyp* mice. Further, we describe the expected mechanical consequences of the final products of mineralization, with resistance to compression and bending at tessellated interfaces in normal WT bone, but slip or creep attributable to the irregular, aborted, mineral volumes in mutant *Hyp* bone.

At this point it seems noteworthy to underscore that the microscale subunit product of these mineralization events – tesselles – guided in their growth by mineral ion availability and noncollagenous proteins, exist not as a solid block-phase of mineral, but rather as discrete abutting entities tessellating throughout bone lamellae. Importantly, this tessellation first arises at the mineralization front from the moment when mature, irregular prolate ellipsoids derived originally from small mineral foci are large and finally abut against one another, while at the same time remaining discrete. Implicit in this growth trajectory is that the tesselles incorporate into and encompass, in a crossfibrillar manner, the collagen fibrils in the collagen bundles within which they grow and mature. While there is indeed some variation in size, particularly near the mineralization front, they generally appear as prolate ellipsoids approximately 0.5-1 µm in diameter when viewed in their shorter dimension, and 2-2.5 µm in length. Of note, these similar dimensions were described in the recent analysis of the "marquise-shaped motifs" found in bone (69). The tessellations are found in all the lamellae we examined, and they appear to occupy only the collagen bundles in which they form, and they do not cross bundle boundaries. When examined by electron microscopy, the tessellations are best viewed by backscattered electron imaging using a smooth, FIB-milled surface near the mineralization front.

4.2 Osteocyte morphology and peri-cellular (peri-lacunar) matrix pliancy

To examine osteocytes, some of our bone samples were preserved under cryo-conditions (high-pressure freezing followed by freeze substitution) to minimize cell shrinkage and other artifacts associated with conventional fixation and embedding protocols. From these samples, additional FIB-SEM volumes were obtained, and deep learning-based segmentation of osteocytes was performed, particularly to discriminate (for segmentation) between cellular and matrix osmium-stained structure. Using this approach, osteocyte processes were observed to extend primarily towards the endosteal and periosteal surfaces similarly in both normal WT and mutant *Hyp* bone. However, alterations in the dendritic cell process morphology became evident between the two samples when local thickness heatmaps were produced, with *Hyp* osteocyte cell processes appearing much thicker. Moreover, in these decalcified samples near the mineralization front where the WT osteocyte existed within fully mineralized matrix (before the decalcification procedure) in its lacuno-canalicular environment, the *Hyp* osteocyte existed in a zone of incompletely mineralized bone replete with its collagen but with noticeably abundant noncollagenous protein matrix (in part excess OPN) in this hypomineralized region of the *Hyp* sample.

This knowledge of osteocyte relations with a surrounding hypomineralized bone matrix in XLH/*Hyp* allows for conjecture about how osteocyte cell signaling might be affected in this disease state. Our work is supported by previous studies showing the well-documented peri-osteocytic lesions (POLs) where unmineralized matrix surrounds entire osteocytes. Steendijk and Boyde noted frequent circumlacunar lesions or unmineralized "lids" of lacunae in the bone of hypophosphatemia rickets patients that appeared together with a disrupted mineralization front, correctly hypothesizing about osteocyte control over mineralization given the minimal evidence at the time (43). Not only do we now know that changes in osteocyte signaling result in profound mineralization defects both locally at peri-lacunar sites in the matrix and in bone as a whole through its role as an endocrine cell pertaining to FGF23 and likely other factors (71), but we are also starting to understand the role that alterations of the peri-lacunar environment (such as in XLH/*Hyp* bone) plays on biomechanics (72). Moreover, osteocytes are central to mechanosensing and bone homeostasis programs, events clearly dysregulated given the altered osteocyte cell geometries within a hypomineralized matrix that we have shown. More generally and unrelated to any pathology, these data also speak to the heterogeneity of the osteocyte cell population. In previous FIB-SEM investigations on osteocytes in normal bone, Hasegawa *et al*. noted thicker, "stout" processes with what could be considered as "distribution hubs" near the mineralization front (the samples were also decalcified) (73). We see evidence of this here as well, particularly in the *Hyp* bone sample residing in the more-pliant, unmineralized matrix. It remains entirely possible, and even likely, that subsets of osteocytes exist before (osteoid osteocytes), at, and beyond the mineralization front where cell morphology and

interactions with matrix and mineral contribute to their gene expression and signaling programs (74). Further investigation using volume-based microscopy methods sensitive enough to discern nanoscale cell geometries such as delicate/thin cell processes, with the sharing of more streamlined protocols between researchers, and using deep-learning approaches for refined analyses, will be key to advancing this topic further.

4.3 A new paradigm for lamellar organization and mineral packing in bone

Given the observations we have made for mineral form and packing at the microscale in bone, we propose to expand the current comprehensive view of the hierarchical organization of normal bone to now include the presence of micrometer-sized crossfibrillar mineral tessellations. It could be considered that evidence for such tessellations might be construed by finer scale observations on the organization of bone mineral such as by descriptions of mineral rosettes by TEM (68) and mineral aggregates by STEM (75). However, beyond this, here we demonstrate in normal bone an extensive and pervasive packing pattern for mineral (true tessellation) at both the nano- and microscale, with discrete, interface-rich packing of mature prolate ellipsoids (tesselles) within ordered collagen arrays. This periodic structuring paradigm for mineral organization differs from the former hypothetical view that mineralization of the extracellular matrix in bone is both generally solid and continuous over the many dimensions beyond the well-characterized mineralization events related to the collagen D-spacing structure (gap/overlap zones). While we have not observed any evidence for ultimate tesselle fusion during their maturation, this possibility deserves further study since such an event would have profound consequences on the stiffness of bones – fusion would likely embrittle them at the material level, such as in hypermineralized senescent bone.

Collagen fibrils within lamellae are organized into distinct bundles – although merging and splitting – which range between 2-3 µm in cross-sectional diameter (70, 76). These three-dimensional collagen bundles co-aligned within one lamella contain a patchwork of tessellated and staggered, packed prolate ellipsoids of slightly differing sizes and irregularity: 3-4 ellipsoids roughly span the transverse dimension of each collagen bundle. The co-existence of the bundles of the collagen phase and the smaller-scale mineral tessellations that populate the bundles is schematically depicted in Fig. 5D. Within each bundle, the longer axes of prolate ellipsoids are co-aligned with their bundle axis, indicating some degree of preferential growth in the longitudinal axis. Any layer of ordered collagen bundles (that are populated by abutting tessellated mineral ellipsoids) and an adjacent layer of ordered collagen bundles

(populated by their own set of mineral ellipsoids) are identical except for having different orientations. Although the periodicity of bone lamellae – as canonically inferred from polarized light microscopy or electron microscopy observations – results from pairs of adjacent layers of bundles combined being 4-6 µm thick (24, 76, 77), we now demonstrate that every such pair consists of angularly offset, nearly identical sublayers, each being 2-3 µm. The assembly of angularly offset layers of parallel bundles that contain submicrometer-sized tessellated ellipsoids is shown in Fig. 5D.

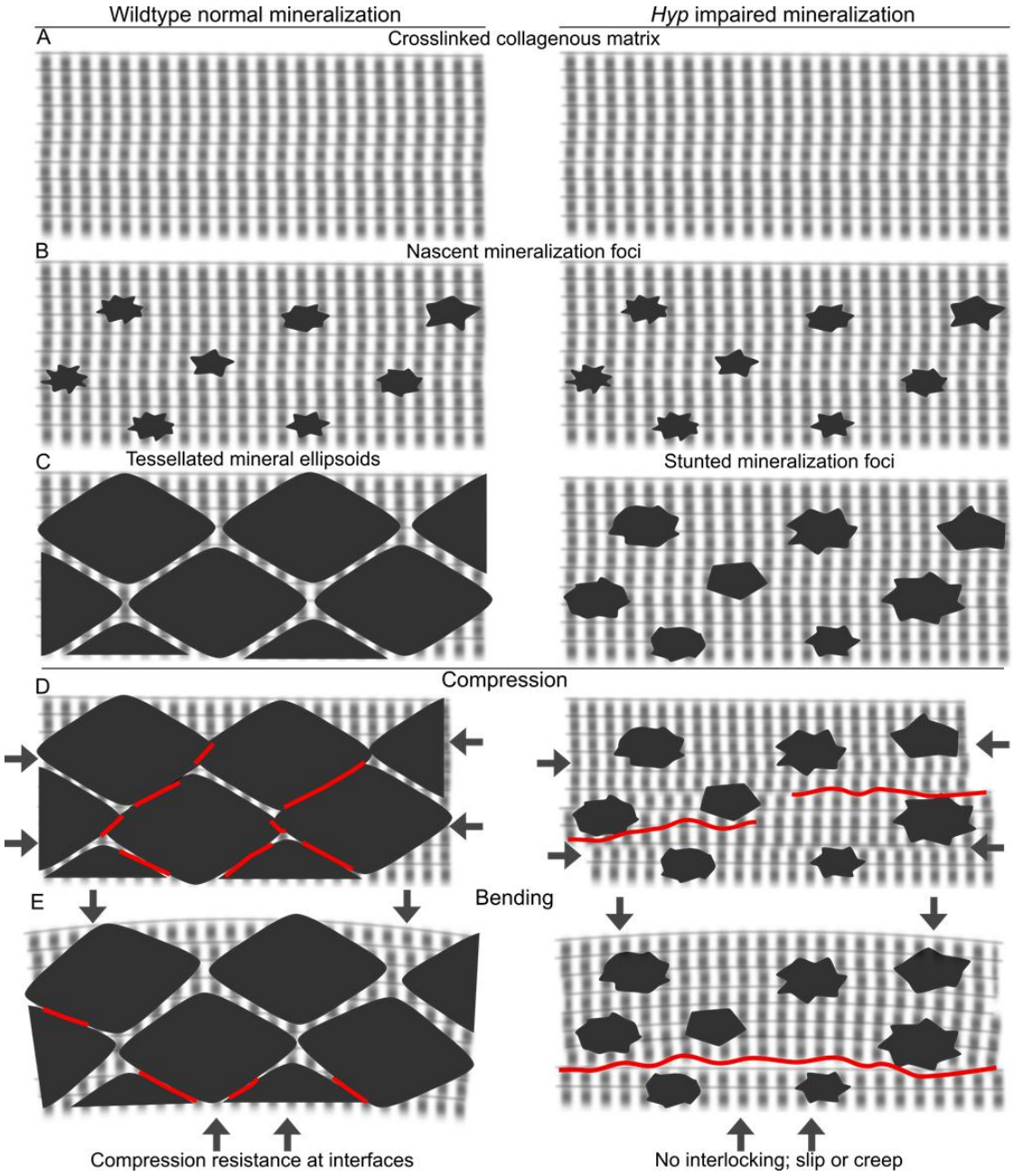

Fig. 7. Mechanistic effect of normal crossfibrillar mineral tessellation and the lack thereof in *Hyp* mice. (A-C) Schematic diagram of the trajectory of mineral nucleation, and mineral foci and mineral ellipsoid growth, in WT and *Hyp* bone. (D,E) Anticipated mechanical behavior of normal and *Hyp* bone under compression and bending stresses. Red boundaries indicate the sites of maximal strain.

4.4 Comparisons with other mineral tessellations in biology

Tessellation is a common theme in Nature, particularly in the field of biomineralization where stiffness and toughness are routinely required. For example, tessellated cartilage or "tesserae" of "abutting, mineralized, hexagonal blocks, are prominent features at the scale of millimeters in the skeleton of elasmobranchs (78). Some members of this family – such as myliobatid stingrays – crush hard mineralized structures in their prey using tessellated "pavement-like tooth plates" (79). In turtles, the carapace of its shell use hierarchically organized, interlocking, alternating rigid and flexible elements to achieve stiffness, strength, and toughness at a low weight (80). Similarly, the armadillo carapace uses tessellated mineral tiles connected by collagen fibers – this proving advantageous for thwarting the keratin-based claws of predators (81). There are many other examples of biological tessellation, and this theme has been used in bioinspired materials design. The "tablet sliding" principle of mineral tessellation as seen in mollusk-shell nacre was used to design a superior impact-resistant glass through internal laser etching (82). Tessellated assemblies with minimal stagger are more adapted for flexibility and toughness, while those with extensive stagger are stiffer (83). In support of this, increases in the mineral content of staggered composites are responsible for larger changes in elastic modulus, as modeled by Bar-On and Wagner (84).

5. Conclusions

This study describes a trajectory and a product of mineral growth in bone from the nano- to the microscale. It also provides for additional understanding of the hierarchical organization of bone at the level of mineral integration with collagen fibril bundles and their organization into lamellae. We also present a new understanding of the periodicity of bone lamellae based on the tessellation feature we describe – an alternative model describing a lamellar periodicity of only 2-3 µm. Additionally we discuss the importance of appropriate development and maintenance of tessellated interfaces, much of which occurs through the inhibitory actions of noncollagenous proteins (such as OPN) and the enzymes that remove them (such as PHEX); as such, we highlight the Stenciling Principle of biomineralization in which the interplay between inhibitory molecules/proteins and tissue-specific enzyme expression (for which the

inhibitory molecules are the substrates) promotes and refines mineralization. Further 3D investigations into the nature of tessellated inorganic-organic arrangements in other normal mineralized tissues will be critical in establishing this as a universal strengthening mechanism. Finally, we describe defective mineral foci and ellipsoid growth in XLH/*Hyp* as interfering with the normal mineral tessellation program such that a mechanistic view of the weakened mechanical properties of osteomalacic bone can be explained. We additionally describe in *Hyp* mice the altered relationship between abnormal early osteocyte morphology and mineral distribution in the osteomalacic extracellular matrix of bone – a circumstance that likely leads to dysregulation of cell signaling important to the homeostasis of healthy bone.

Acknowledgements

This study was supported by a grant from the Canadian Institutes of Health Research to MDM (MOP-142330). This work was also supported funding from the provincial FRQS Network for Oral and Bone Health Research. From McGill University, we thank Dr. Kelly Sears and Ms. Weawkamol Leelapornpisit of the Facility for Electron Microscopy Research for assistance with the FIB-SEM work, and Dr. Rui Tahara of the Cell Imaging and Analysis Network core facility of the Integrated Qualitative Biology Initiative for assistance with the µCT work, and Jacob Reznikov for video editing. From Object Research Systems Inc, we thank Benjamin Provencher for his help with deep-learning protocols and applications. Marc McKee is the Canada Research Chair in Biomineralization, and his research was undertaken, in part, thanks to funding from the Canada Research Chairs program.

Conflicts of Interest / Disclosures

Natalie Reznikov discloses that she consults for Object Research Systems Inc. in Montreal, but has no financial stake in the company.

CRediT contributions

Daniel Buss: Conceptualization, Methodology, Formal analysis, Investigation, Writing - Original draft, Writing - Review and editing, Visualization. **Natalie Reznikov**: Conceptualization, Methodology, Formal analysis, Investigation, Writing - Review and editing, Visualization. **Marc McKee**: Conceptualization, Methodology, Formal analysis, Investigation, Data curation, Writing - Review and editing, Supervision, Project administration, Funding acquisition.

References

1. Reznikov N, Steele JAM, Fratzl P, Stevens MM. A materials science vision of extracellular matrix mineralization. Nature Reviews Materials. 2016;1(8).
2. Addison WN, Azari F, Sorensen ES, Kaartinen MT, McKee MD. Pyrophosphate inhibits mineralization of osteoblast cultures by binding to mineral, up-regulating osteopontin, and inhibiting alkaline phosphatase activity. J Biol Chem. 2007;282(21):15872-83.
3. Fleisch H, Bisaz S. Mechanism of calcification: inhibitory role of pyrophosphate. Nature. 1962;195:911.
4. Roberts F, Zhu D, Farquharson C, Macrae VE. ENPP1 in the Regulation of Mineralization and Beyond. Trends Biochem Sci. 2019;44(7):616-28.
5. Orriss IR. Extracellular pyrophosphate: The body's "water softener". Bone. 2020:115243.
6. Brylka L, Jahnen-Dechent W. The role of fetuin-A in physiological and pathological mineralization. Calcif Tissue Int. 2013;93(4):355-64.

7. Reznikov N, Hoac B, Buss D, Addison W, Barros N, McKee M. Biological stenciling of mineralization in the skeleton: Local enzymatic removal of inhibitors in the extracellular matrix. Bone. 2020.
8. Robey P.G. BAL. Extracellular Matrix and Biomineralization of Bone. Primer on the Metabolic Bone Diseases and Disorders of Mineral Metabolism American Society of Bone and Mineral Research 2003. p. 38-46.
9. McKee MD, Nanci A. Osteopontin: an interfacial extracellular matrix protein in mineralized tissues. Connect Tissue Res. 1996;35(1-4):197-205.
10. Staines KA, MacRae VE, Farquharson C. The importance of the SIBLING family of proteins on skeletal mineralisation and bone remodelling. J Endocrinol. 2012;214(3):241-55.
11. Addison WN, Masica DL, Gray JJ, McKee MD. Phosphorylation-dependent inhibition of mineralization by osteopontin ASARM peptides is regulated by PHEX cleavage. J Bone Miner Res. 2010;25(4):695-705.
12. Hoac B, Nelea V, Jiang W, Kaartinen MT, McKee MD. Mineralization-inhibiting effects of transglutaminase-crosslinked polymeric osteopontin. Bone. 2017;101:37-48.
13. Yuan Q, Jiang Y, Zhao X, Sato T, Densmore M, Schuler C, et al. Increased osteopontin contributes to inhibition of bone mineralization in FGF23-deficient mice. J Bone Miner Res. 2014;29(3):693-704.
14. Sorensen ES, Hojrup P, Petersen TE. Posttranslational modifications of bovine osteopontin: identification of twenty-eight phosphorylation and three O-glycosylation sites. Protein Sci. 1995;4(10):2040-9.
15. Narisawa S, Yadav MC, Millan JL. In vivo overexpression of tissue-nonspecific alkaline phosphatase increases skeletal mineralization and affects the phosphorylation status of osteopontin. J Bone Miner Res. 2013;28(7):1587-98.
16. McKee MD, Nanci A. Osteopontin at mineralized tissue interfaces in bone, teeth, and osseointegrated implants: ultrastructural distribution and implications for mineralized tissue formation, turnover, and repair. Microsc Res Tech. 1996;33(2):141-64.
17. Scherft JP. The lamina limitans of the organic matrix of calcified cartilage and bone. J Ultrastruct Res. 1972;38(3):318-31.
18. Barros NM, Hoac B, Neves RL, Addison WN, Assis DM, Murshed M, et al. Proteolytic processing of osteopontin by PHEX and accumulation of osteopontin fragments in Hyp mouse bone, the murine model of X-linked hypophosphatemia. J Bone Miner Res. 2013;28(3):688-99.
19. Currey JD. The Mechanical Adaptations of Bones. Princeton, New Jersey: Princeton University Press; 1984.
20. Marino AA, Becker RO, Bachman CH. Dielectric determination of bound water of bone. Phys Med Biol. 1967;12(3):367-78.
21. Timmins PA, Wall JC. Bone water. Calcif Tissue Res. 1977;23(1):1-5.
22. Turov VV, Gun'ko VM, Zarko VI, Leboda R, Jablonski M, Gorzelak M, et al. Weakly and strongly associated nonfreezable water bound in bones. Colloids Surf B Biointerfaces. 2006;48(2):167-75.
23. Nylen MU, Scott DB, M. MV. Mineralization of turkey leg tendon. II. Collagen-mineral relations revealed by electron and X-ray microscopy. . 1960.
24. Ascenzi A, Bonucci E, Bocciarelli DS. An Electron Microscope Study of Osteon Calcification. J Ultrastruct Res. 1965;12:287-303.
25. Landis WJ, Song MJ, Leith A, McEwen L, McEwen BF. Mineral and organic matrix interaction in normally calcifying tendon visualized in three dimensions by high-voltage electron microscopic tomography and graphic image reconstruction. J Struct Biol. 1993;110(1):39-54.
26. Weiner S, Traub W. Organization of hydroxyapatite crystals within collagen fibrils. FEBS Lett. 1986;206(2):262-6.
27. Kim D, Lee B, Thomopoulos S, Jun YS. The role of confined collagen geometry in decreasing nucleation energy barriers to intrafibrillar mineralization. Nat Commun. 2018;9(1):962.
28. Landis WJ, Jacquet R. Association of calcium and phosphate ions with collagen in the mineralization of vertebrate tissues. Calcif Tissue Int. 2013;93(4):329-37.
29. McNally EA, Schwarcz HP, Botton GA, Arsenault AL. A model for the ultrastructure of bone based on electron microscopy of ion-milled sections. PLoS One. 2012;7(1):e29258.
30. Boyde A, Jones S. Aspects of Anatomy and Development of Bone. Advances in Organ Biology. 1998;5A:3-44.

31. Schwarcz HP. The ultrastructure of bone as revealed in electron microscopy of ion-milled sections. Semin Cell Dev Biol. 2015;46:44-50.
32. Hasegawa T. Ultrastructure and biological function of matrix vesicles in bone mineralization. Histochem Cell Biol. 2018;149(4):289-304.
33. Hu YY, Rawal A, Schmidt-Rohr K. Strongly bound citrate stabilizes the apatite nanocrystals in bone. Proc Natl Acad Sci U S A. 2010;107(52):22425-9.
34. Murshed M. Mechanism of Bone Mineralization. Cold Spring Harb Perspect Med. 2018;8(12).
35. Wang Y, Von Euw S, Fernandes FM, Cassaignon S, Selmane M, Laurent G, et al. Water-mediated structuring of bone apatite. Nat Mater. 2013;12(12):1144-53.
36. Termine JD, Posner AS. Amorphous/crystalline interrelationships in bone mineral. Calcif Tissue Res. 1967;1(1):8-23.
37. Bocciarelli DS. Morphology of crystallites in bone. Calcif Tissue Res. 1970;5(3):261-9.
38. Reznikov N, Almany-Magal R, Shahar R, Weiner S. Three-dimensional imaging of collagen fibril organization in rat circumferential lamellar bone using a dual beam electron microscope reveals ordered and disordered sub-lamellar structures. Bone. 2013;52(2):676-83.
39. You L, Cowin SC, Schaffler MB, Weinbaum S. A model for strain amplification in the actin cytoskeleton of osteocytes due to fluid drag on pericellular matrix. J Biomech. 2001;34(11):1375-86.
40. Santos A, Bakker AD, Klein-Nulend J. The role of osteocytes in bone mechanotransduction. Osteoporos Int. 2009;20(6):1027-31.
41. Millan JL, Whyte MP. Alkaline Phosphatase and Hypophosphatasia. Calcif Tissue Int. 2016;98(4):398-416.
42. Boukpessi T, Hoac B, Coyac BR, Leger T, Garcia C, Wicart P, et al. Osteopontin and the dento-osseous pathobiology of X-linked hypophosphatemia. Bone. 2017;95:151-61.
43. Steendijk R, Boyde A. Scanning electron microscopic observations on bone from patients with hypophosphataemic (vitamin D resistant) rickets. Calcif Tissue Res. 1973;11(3):242-50.
44. McKee MD, Hoac B, Addison WN, Barros NM, Millan JL, Chaussain C. Extracellular matrix mineralization in periodontal tissues: Noncollagenous matrix proteins, enzymes, and relationship to hypophosphatasia and X-linked hypophosphatemia. Periodontol 2000. 2013;63(1):102-22.
45. Addison WN, Nakano Y, Loisel T, Crine P, McKee MD. MEPE-ASARM peptides control extracellular matrix mineralization by binding to hydroxyapatite: an inhibition regulated by PHEX cleavage of ASARM. J Bone Miner Res. 2008;23(10):1638-49.
46. Malick LE, Wilson RB. Modified thiocarbohydrazide procedure for scanning electron microscopy: routine use for normal, pathological, or experimental tissues. Stain Technol. 1975;50(4):265-9.
47. Chissoe WF, Vezey EL, Skvarla JJ. The Use of Osmium-Thiocarbohydrazide for Structural Stabilization and Enhancement of Secondary Electron Images in Scanning Electron Microscopy of Pollen. Grana. 1995;34(5):317-24.
48. Reznikov N, Buss D, Provencher B, McKee M, Piche N. Deep learning and 3D imaging in structural biology. Journal of Structural Biology. 2020.
49. Ohata Y, Ozono K. [Updates on rickets and osteomalacia: guidelines for diagnosis of rickets and osteomalacia]. Clin Calcium. 2013;23(10):1421-8.
50. Eicher EM, Southard JL, Scriver CR, Glorieux FH. Hypophosphatemia: mouse model for human familial hypophosphatemic (vitamin D-resistant) rickets. Proc Natl Acad Sci U S A. 1976;73(12):4667-71.
51. McKee MD, Nanci A. Postembedding colloidal-gold immunocytochemistry of noncollagenous extracellular matrix proteins in mineralized tissues. Microsc Res Tech. 1995;31(1):44-62.
52. Bonucci E, Silvestrini G, Di Grezia R. The ultrastructure of the organic phase associated with the inorganic substance in calcified tissues. Clin Orthop Relat Res. 1988(233):243-61.
53. Rauch F. Material matters: a mechanostat-based perspective on bone development in osteogenesis imperfecta and hypophosphatemic rickets. J Musculoskelet Neuronal Interact. 2006;6(2):142-6.
54. Tang T, Wagermaier W, Schuetz R, Wang Q, Eltit F, Fratzl P, et al. Hypermineralization in the femoral neck of the elderly. Acta Biomater. 2019;89:330-42.

55. Carpenter TO, Shaw NJ, Portale AA, Ward LM, Abrams SA, Pettifor JM. Rickets. Nat Rev Dis Primers. 2017;3:17101.
56. Zhang C, Zhao Z, Sun Y, Xu L, JiaJue R, Cui L, et al. Clinical and genetic analysis in a large Chinese cohort of patients with X-linked hypophosphatemia. Bone. 2019;121:212-20.
57. Strom TM, Francis F, Lorenz B, Boddrich A, Econs MJ, Lehrach H, et al. Pex gene deletions in Gy and Hyp mice provide mouse models for X-linked hypophosphatemia. Hum Mol Genet. 1997;6(2):165-71.
58. Shanbhogue VV, Hansen S, Folkestad L, Brixen K, Beck-Nielsen SS. Bone geometry, volumetric density, microarchitecture, and estimated bone strength assessed by HR-pQCT in adult patients with hypophosphatemic rickets. J Bone Miner Res. 2015;30(1):176-83.
59. Bonivtch AR, Bonewald LF, Nicolella DP. Tissue strain amplification at the osteocyte lacuna: a microstructural finite element analysis. J Biomech. 2007;40(10):2199-206.
60. McKee MD, Nanci A, Landis WJ, Gotoh Y, Gerstenfeld LC, Glimcher MJ. Developmental appearance and ultrastructural immunolocalization of a major 66 kDa phosphoprotein in embryonic and post-natal chicken bone. Anat Rec. 1990;228(1):77-92.
61. Finean JB, Engstrom A. The low-angle scatter of x-rays from bone tissue. Biochim Biophys Acta. 1953;11(2):178-89.
62. McKee MD, Nanci A. Osteopontin and the bone remodeling sequence. Colloidal-gold immunocytochemistry of an interfacial extracellular matrix protein. Ann N Y Acad Sci. 1995;760:177-89.
63. Beck GR, Jr., Zerler B, Moran E. Phosphate is a specific signal for induction of osteopontin gene expression. Proc Natl Acad Sci U S A. 2000;97(15):8352-7.
64. Fatherazi S, Matsa-Dunn D, Foster BL, Rutherford RB, Somerman MJ, Presland RB. Phosphate regulates osteopontin gene transcription. J Dent Res. 2009;88(1):39-44.
65. Bertazzo S, Bertran, C.A., Camilli, J.A. . Morphological Characterization of Femur and Parietal Bone Mineral of Rats at Different Ages. Key Engineering Materials. 2005:309-11.
66. Midura RJ, Vasanji A, Su X, Midura SB, Gorski JP. Isolation of calcospherulites from the mineralization front of bone. Cells Tissues Organs. 2009;189(1-4):75-9.
67. Midura RJ, Vasanji A, Su X, Wang A, Midura SB, Gorski JP. Calcospherulites isolated from the mineralization front of bone induce the mineralization of type I collagen. Bone. 2007;41(6):1005-16.
68. Grandfield K, Vuong V, Schwarcz HP. Ultrastructure of Bone: Hierarchical Features from Nanometer to Micrometer Scale Revealed in Focused Ion Beam Sections in the TEM. Calcif Tissue Int. 2018;103(6):606-16.
69. Shah FAR, K. Palmquist, A. . Transformation of bone mineral morphology: From discrete marquise-shaped motifs to a continuous interwoven mesh. Bone Reports. 2020.
70. Reznikov N, Shahar R, Weiner S. Three-dimensional structure of human lamellar bone: the presence of two different materials and new insights into the hierarchical organization. Bone. 2014;59:93-104.
71. Dallas SL, Prideaux M, Bonewald LF. The osteocyte: an endocrine cell ... and more. Endocr Rev. 2013;34(5):658-90.
72. Kaya S, Basta-Pljakic J, Seref-Ferlengez Z, Majeska RJ, Cardoso L, Bromage TG, et al. Lactation-Induced Changes in the Volume of Osteocyte Lacunar-Canalicular Space Alter Mechanical Properties in Cortical Bone Tissue. J Bone Miner Res. 2017;32(4):688-97.
73. Hasegawa T, Yamamoto T, Hongo H, Qiu Z, Abe M, Kanesaki T, et al. Three-dimensional ultrastructure of osteocytes assessed by focused ion beam-scanning electron microscopy (FIB-SEM). Histochem Cell Biol. 2018;149(4):423-32.
74. Dallas SL, Bonewald LF. Dynamics of the transition from osteoblast to osteocyte. Ann N Y Acad Sci. 2010;1192:437-43.
75. Reznikov N, Bilton M, Lari L, Stevens MM, Kroger R. Fractal-like hierarchical organization of bone begins at the nanoscale. Science. 2018;360(6388).
76. Boyde A, Hobdell MH. Scanning electron microscopy of primary membrane bone. Z Zellforsch Mikrosk Anat. 1969;99(1):98-108.
77. Currey JD. Bones : structure and mechanics. Princeton, New Jersey ;: Princeton University Press; 2002.
78. Dean MN, Mull CG, Gorb SN, Summers AP. Ontogeny of the tessellated skeleton: insight from the skeletal growth of the round stingray Urobatis halleri. J Anat. 2009;215(3):227-39.

79. Fratzl P, Kolednik O, Fischer FD, Dean MN. The mechanics of tessellations - bioinspired strategies for fracture resistance. Chem Soc Rev. 2016;45(2):252-67.
80. Achrai B, Wagner HD. The turtle carapace as an optimized multi-scale biological composite armor - A review. J Mech Behav Biomed Mater. 2017;73:50-67.
81. Chen IH, Kiang JH, Correa V, Lopez MI, Chen PY, McKittrick J, et al. Armadillo armor: mechanical testing and micro-structural evaluation. J Mech Behav Biomed Mater. 2011;4(5):713-22.
82. Yin Z, Hannard F, Barthelat F. Impact-resistant nacre-like transparent materials. Science. 2019;364(6447):1260-3.
83. Gao C, Hasseldine BPJ, Li L, Weaver JC, Li Y. Amplifying Strength, Toughness, and Auxeticity via Wavy Sutural Tessellation in Plant Seedcoats. Adv Mater. 2018:e1800579.
84. Bar-On B, Wagner HD. The emergence of an unusual stiffness profile in hierarchical biological tissues. Acta Biomater. 2013;9(9):8099-109.